



**HAL**  
open science

## Dose area product primary standards established by graphite calorimetry at the LNE-LNHB for small radiation fields in radiotherapy

Julien Jurczak, Benjamin Rapp, Franck Delaunay, Jean Gouriou, Stéphane Dufreneix, jean-marc bordy

### ► To cite this version:

Julien Jurczak, Benjamin Rapp, Franck Delaunay, Jean Gouriou, Stéphane Dufreneix, et al.. Dose area product primary standards established by graphite calorimetry at the LNE-LNHB for small radiation fields in radiotherapy. *Physica Medica European Journal of Medical Physics*, 2022, 98, pp.18-27. 10.1016/j.ejmp.2022.03.013 . hal-03951460

**HAL Id: hal-03951460**

**<https://hal.science/hal-03951460>**

Submitted on 23 Jan 2023

**HAL** is a multi-disciplinary open access archive for the deposit and dissemination of scientific research documents, whether they are published or not. The documents may come from teaching and research institutions in France or abroad, or from public or private research centers.

L'archive ouverte pluridisciplinaire **HAL**, est destinée au dépôt et à la diffusion de documents scientifiques de niveau recherche, publiés ou non, émanant des établissements d'enseignement et de recherche français ou étrangers, des laboratoires publics ou privés.

# ***Dose Area Product primary standards established by graphite calorimetry at the LNE-LNHB for small radiation fields in radiotherapy***

Julien Jurczak<sup>a,\*</sup>, Benjamin Rapp<sup>a</sup>, Frank Delaunay<sup>a</sup>, Jean Gouriou<sup>a</sup>, Stéphane Dufreneix<sup>a,b</sup>, Jean-Marc Bordy<sup>a</sup>

a Université Paris-Saclay, CEA, List, Laboratoire National Henri Becquerel (LNE-LNHB), F-91120 Palaiseau, France

b Institut de Cancérologie de l'Ouest, Angers, France

## **1 Introduction**

Use of small fields is becoming standard in actual treatment modalities such as intensity-modulated radiotherapy (IMRT), volumetric-modulated arctherapy (VMAT) and stereotactic radiotherapy (SRT) thanks to the generalized availability of multileaf collimators (MLC). In particular, SRT is a widely used state-of-the-art technique combining high doses in small volumes accurately targeted, allowing a better sparing of surrounding healthy tissues. Initially developed to treat brain lesions [1,2], its use has been extended to all types of extra-cranial lesions (lung, liver, prostate, ...) [3–5] with irradiation fields as small as 4 mm. So far, primary standards for high-energy photons in radiotherapy are established in a 10 x 10 cm<sup>2</sup> field size at 10 g.cm<sup>-2</sup> depth in terms of absorbed dose to water at a point, according to recommendations of international dosimetric protocols [6,7]. These protocols, published more than two decades ago and updated a few times to include new dosimeters, are used today in the absence of primary standards adapted to current clinical conditions

Similarly, the emergence of specialized radiation delivery units (GammaKnife<sup>®</sup>, Tomotherapy<sup>®</sup>, Cyberknife<sup>®</sup>, and more recently MR-linacs, ZAP-X<sup>®</sup>) for which the conventional reference 10 x 10 cm<sup>2</sup> field size and 100 cm source-to-surface distance (SSD) or source-to-detector (SDD) conditions are not applicable underlined the need of a new formalism for reference dosimetry of small fields [8]. Consequently, a joint IAEA-AAPM code of practice named TRS 483 was developed to standardize guidance for dosimetry of small static fields used in external beam radiotherapy [9]. Relative dosimetry in particular through field output factors (OF), which account for differences between reference and clinical field sizes conditions, is extensively discussed. Indeed, contrary to usual broad beams, OF cannot be accurately approximated as the ratio of detector readings and a field output correction factor depending on machine, beam quality, detector and field size-dependant perturbations has to be used [10–13]. TRS 483 provides an extensive set of correction factors with comprehensive data up to 2015 but some are still subject to debate [14].

The French primary dosimetry standards laboratory (PDSL) LNE-LNHB began to study the metrology in small beams with the construction of a new absorbed dose standard, the GR10 graphite calorimeter [15], with a small sensitive element ( $\varnothing_{\text{core}} = 6$  mm). By calibrating a small volume ionization chamber Exradin A1SL, reference in term of absorbed dose to water at a point in a 2 x 2 cm<sup>2</sup> field has been established

[16] and it has been shown that the calibration coefficient was relatively independent of the field size between 10 x 10 cm<sup>2</sup> and 2 x 2 cm<sup>2</sup>. Below 2 x 2 cm<sup>2</sup>, the traceability of the measured dose to a national standard of absorbed dose to water at a point is no longer demonstrated, leading to an increased uncertainty of dose delivery. The technological limits of standards miniaturization having been reached, it was necessary to revisit the present paradigm of dose at a point as the reference quantity for reference radiotherapy dosimetry. Quite easily measurable in homogeneous large field sizes and conceptually understandable from a macroscopic point of view, its use for sub-centimeter beams becomes problematic.

The approach proposed by LNE-LNHB consists in performing an integrated measurement over an area larger than the irradiation field through another quantity: the Dose Area Product (DAP) [17]. While this concept has been investigated for output factor measurements [17–21] as well as beam quality parameter [22–24], the major innovation introduced by LNE-LNHB is the DAP use as a reference quantity for small field dosimetry..

This work was initiated by the construction of the GR11 graphite calorimeter with a 30 mm diameter core [25]. The transfer of the primary standards in terms of DAP to the end user needs transfer dosimeters with the same sensitive area than the GR11 graphite calorimeter core. A previous work investigated DAP primary standards measurements for three circular fields with a first in-house designed plane-parallel ionization chamber [26]. Some technical difficulties were encountered such as sealing defects of the chamber and the significant deformation of the collection volume due to water pressure. Those difficulties associated with the limited number of studied field sizes made a final conclusion difficult to reach.

This paper describes the validation of the Monte Carlo calculations required for the determination of correction factors in small fields. Two new plane-parallel ionization chambers built in-house from the same plans, and to be used as reference detectors for DAP measurements are compared. Finally, new DAP standards for a more extensive set of square and circular small fields up to 15 mm side length or diameter respectively are presented.

## 2 Material and methods

### 2.1 Formalism

Establishment of primary standards for small fields in terms of Dose Area Product by graphite calorimetry is obtained by calibrating a DAP reference ionization chamber in water from the integrated dose over the core area of the large section calorimeter, at a source distance of 100 cm and 10 g.cm<sup>-2</sup> depth. The calibration coefficient  $N_{DAP,w}$  (in Gy.cm<sup>2</sup>.C<sup>-1</sup>) is expressed as :

$$N_{DAP,w} = \frac{DAP_{w/Mon}}{Q_{w/Mon}^*} = \frac{D_{core/Mon}}{Q_{w/Mon}^*} \left[ \frac{D_w(V_{core})}{D_{core}} \right]_{MC} S_{core} k_i \quad \#(1)$$

where:

- $D_{core/Mon}$  is the average absorbed dose in the core (sensitive part) of the large section calorimeter normalized to the monitor ionization chamber
- $Q_{w/Mon}^*$  is the charge measured by the reference ionization chamber corrected for polarization and recombination effects normalized to the monitor ionization chamber. The integration area being a critical quantity of the DAP, a 2D dose integral correction  $k_{int}$  is introduced to take into account the difference in the deposited energy measured between the core and the collection area of the DAP ionization chamber, related to their possible area differences (see Section 2.5.2). The corrected charge  $Q_w^*$  is then defined as:  $Q_w^* = Q_w \times k_{rec} \times k_{pol} \times k_{int}$  which  $Q_w$  charge measured by the reference ionization chamber in a 30 cm x 30 cm x 30 cm water-filled tank volume (denoted as water phantom afterwards) and corrected for influence quantities: temperature, pressure, humidity;  $[D_w(V_{core}) / D_{core}]_{MC}$  is the graphite to water dose conversion factor calculated by Monte Carlo as the ratio of the average absorbed dose to water in a water volume similar in shape, dimensions and position to the graphite core volume  $V_{core}$  and the average dose in the core  $D_{core}$ ;
- $S_{core}$  is the graphite core area (perpendicular to the beam direction);
- The impurity correction factor  $k_i$  takes into account the effects on the absorbed dose to the core of all the impurities within the core that are different from graphite (thermistors, resin and kapton). This correction was considered here dosimetrically negligible because thermistors are located at the periphery of the core and are not in the direct beam. So it was taken equal to unity, with an uncertainty of 0.1%.

## 2.2 Methodology

This work has been carried out in the 6 MV FFF beam of the Varian TrueBeam linear accelerator at the LNE-LNHB laboratory. The GR11 calorimeter inside its graphite phantom and the water phantom with the DAP chamber to be calibrated were on the treatment table with the original carbon sheet replaced with a more rigid aluminium one. Measurements have been made during four campaigns, with an irradiation time of 120 s and at the maximum dose rate of 14 Gy/min. The gantry was set at a 90 degree angle to exactly control the 10 cm reference depth of the DAP chamber in the water phantom, which is not possible at a 0 degree angle due to disturbances on the water surface. The calorimeter core center was positioned at a distance of 100 cm from the source, at a measurement depth of 10 g.cm<sup>-2</sup> in graphite, achieved by superimposing slices of the phantom at the front of the calorimeter.

The DAP ionization chamber was positioned under the same reference conditions in the water phantom, considering its reference point at the centre of the inner surface of the entrance window. An illustration is presented in **Figure 1**. In order to investigate a potential dependence of the calibration coefficient with the field shape, two types of collimations were studied: square fields of 5; 7; 10; 13 and 15 mm side length defined with jaws, and circular fields of 5; 7.5; 10; 13 and 15 mm diameter defined with additional collimators. Uncertainties were estimated by using the Guide to the expression of Uncertainty in Measurements (GUM) report [27]. Unless otherwise stated, they are given for  $k = 1$  (one standard deviation).

DAP ionization chamber

Water phantom  
(30x30x30 cm<sup>3</sup>)

GR11 graphite  
calorimeter inside its  
graphite phantom

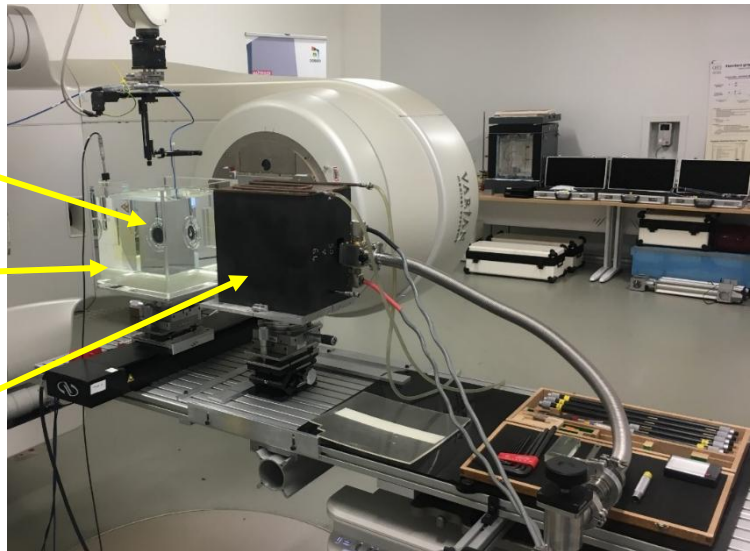


**Figure 1.** Experimental set-up for primary standards establishment in DAP by graphite calorimetry.

Circular fields were defined using Tungsten collimators specifically designed for this work, which were fixed on the base plate of an electron applicator and were slid into an adjustable box using a system of six micrometric screws (see **Figure 2**) to properly manage the critical alignment and centering of the collimator with the beam axis. In addition, a camera fixed on a goniometric support allowing movements along six axes was used. Positioning reproducibility of the collimator lead to a charge measurement variation smaller than 0.1%.



**Figure 2.** Tungsten circular collimator mounted on the exit of the treatment head.

Calorimetric and ionometric measurements were made successively by moving longitudinally the table without modifying the beam collimation. They were normalized to the monitor reading (see Eq.1), giving the link between the two measurements.

For circular fields, a machine field size larger than the largest circular collimators (15 mm diameter) needed to be defined and a square field size of 3 cm side length was realized with jaws. To improve the reliability of the monitoring system and in addition to the internal monitor ionization chamber, two external monitor ionization chambers Exradin A12S denoted “Mon1” and “Mon2” were set horizontally and tangentially to the irradiation field at the treatment head exit to be used as external monitor

ionization chamber. Mon1 and Mon2 were located between the additional collimators and the output of the treatment head. All signals from the external monitors were corrected for influence quantities. Therefore, it was possible to normalize the measurements indifferently with respect to either the internal monitor or Mon1 or Mon2.

For the square fields, it was not possible to use the external monitor ionization chambers without disturbing the beam, so only the internal monitor ionization chamber was used. For both cases, calorimetric measurements were systematically surrounded by ionometric measurements at the beginning and end of the day.

### 2.3 Graphite calorimetry

The GR11 calorimeter is based on the same principle as the former generations of LNE-LNHB graphite calorimeters [15,28,29]. It is made up of three concentric bodies: the core, the jacket and the shield, all embedded inside a fourth body, the block, of the same reference material. In order to minimize heat transfer phenomena between the bodies and its external environment and to ensure that the temperature increase measured is strictly proportional to the energy imparted into the medium, a good thermal insulation is ensured by vacuum gaps between the bodies. The core, the sensitive element, is a flat cylinder of  $(2.919 \pm 0.01)$  mm thickness and  $(30.003 \pm 0.01)$  mm diameter where the temperature rise induced by irradiation is measured by thermistors. Six thermistors are embedded in the core for the measurements, the thermal remote control and the electrical calibration. They are in the form of glass-coated beads of 0.35 mm diameter. More details about the large section calorimeter construction can be found in details in [25] and radiographies are presented in *Figure 3*.

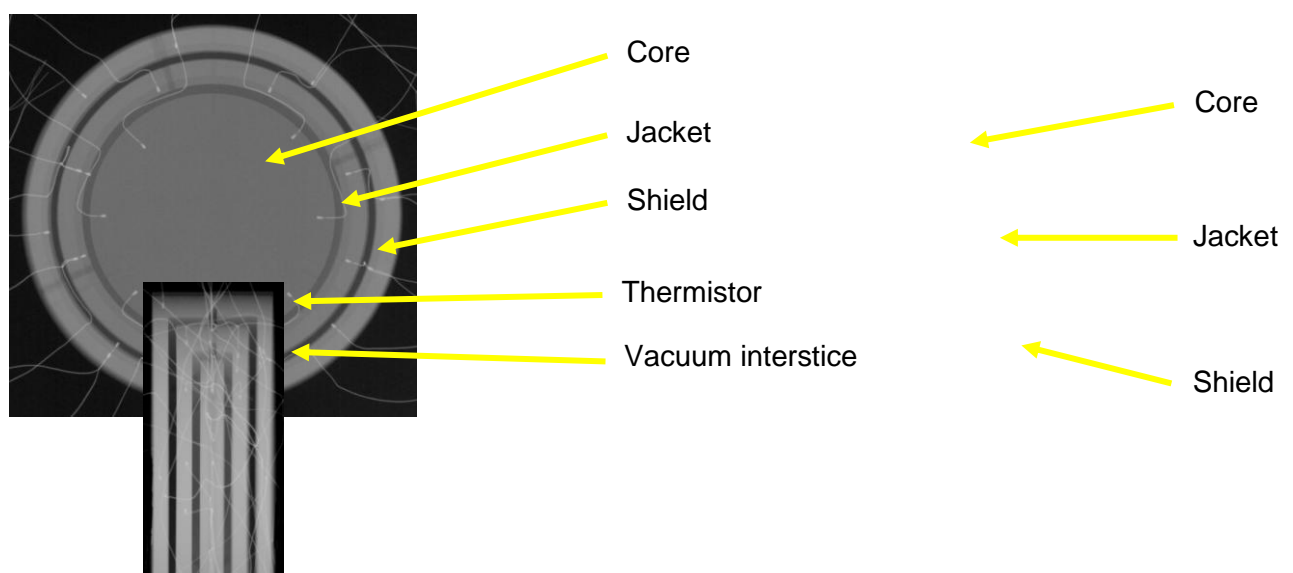


**Figure 3.** Radiographies of the three internal bodies of the GR11 graphite calorimeter from the front (left) and from the side (right).

The graphite calorimeter can be operated in constant-temperature mode or in quasi-adiabatic mode as described in [28]. In constant-temperature mode, the three bodies are maintained at a fixed temperature with the help of heating thermistors by

supplying energy dissipated by Joule effect. Under irradiation, the temperature rise in the core is compensated by a decrease of the electric power dissipated into the other bodies. The absorbed power due to irradiation is then the difference between the electrical power without and with irradiation. In quasi-adiabatic mode, a feedback loop of the shield temperature to that of the core is set up allowing the temperature of all the bodies to grow continuously throughout irradiation and an electrical calibration is required in order to link the temperature rise to the absorbed dose  $D_{core}$  [30]. This last operating mode was used to carry out the calorimetric measurements presented in this article. Temperature rise measurements were between 0.7 and 8.1 mK for the different field sizes considered, with a statistical uncertainty in the range of 0.01 to 0.12%, decreasing with the temperature rise magnitude. As an illustration, the temperature rise curves for the smaller (5 mm) and the larger (15 mm) circular field size diameters are reported in **Figure 4**.

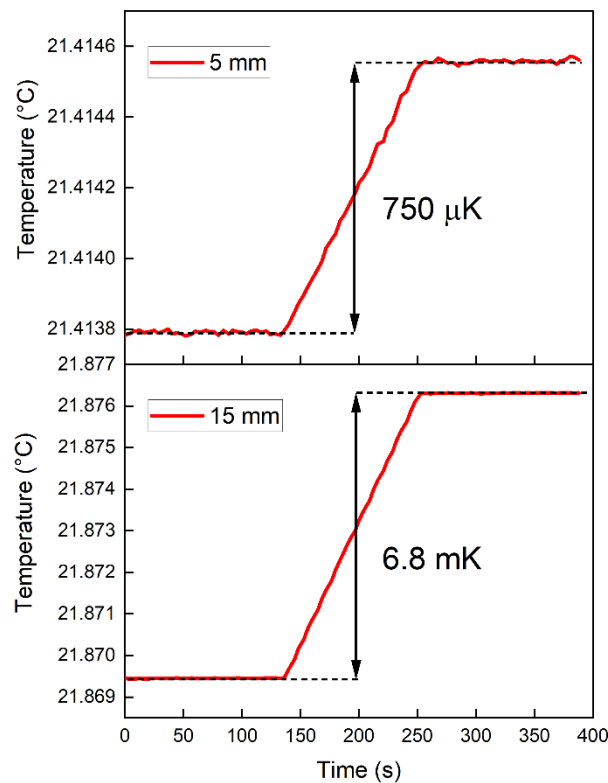


**Figure 4.** Example of temperature rise curves measured for circular field of 5 mm (top) and 15 mm diameter (bottom).

## 2.4 DAP ionization chamber

The DAP ionization chamber is a vented waterproof plane-parallel ionization chamber (see **Figure 5**). The cylindrical cross-linked polystyrene body has an outer diameter of 100 mm with an internal cylindrical air cavity of 2 mm thick nominally. The entrance window has a thickness of 3.5 mm, made of 2.5 mm cross-linked polystyrene and 1 mm external graphite electrode. The graphite-collecting electrode in front of the entrance window has a diameter of 29.5 mm. A 0.5 mm thick guard ring guards the sensitive volume. It leads to a collection area diameter, defined by the area of the collecting electrode plus half the gap between the collecting and guard electrode, of

30 mm. An operating voltage of + 200 V was used, in accordance with usual practice of 100 V per mm of air cavity to get an efficient ionization chamber regime.

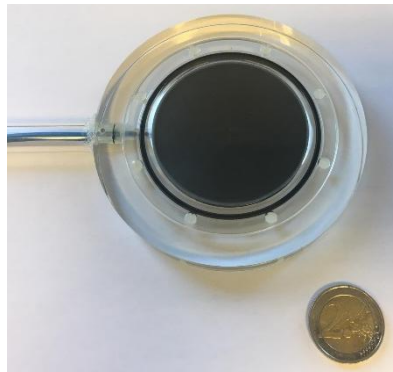


**Figure 5.** DAP ionization chamber.

The assembly accuracy of the two DAP ionization chambers was checked by high-resolution X-ray tomography (XT H 320 large cabinet microfocus CT, Nikon Metrology CT) with voxels of 0.071 mm side length. The high-resolution was needed to distinguish slight radius variations for the 2D dose integral correction determination (see Section 2.5.2). A 2D-view radiography can be found in **Figure 6**. A slight deformation of the cover can be noticed due to a bending on the edges during the screws tightening, leading to a maximum additional air height of 1 mm at center between the cover and the external electrode. This defect has no anisotropy impact on the collecting volume because the average air gap thickness remains constant over the 30 mm diameter collecting area. Furthermore, one can imagine that water pressure on the cover when the chamber is immersed in the water phantom might reduce that volume.

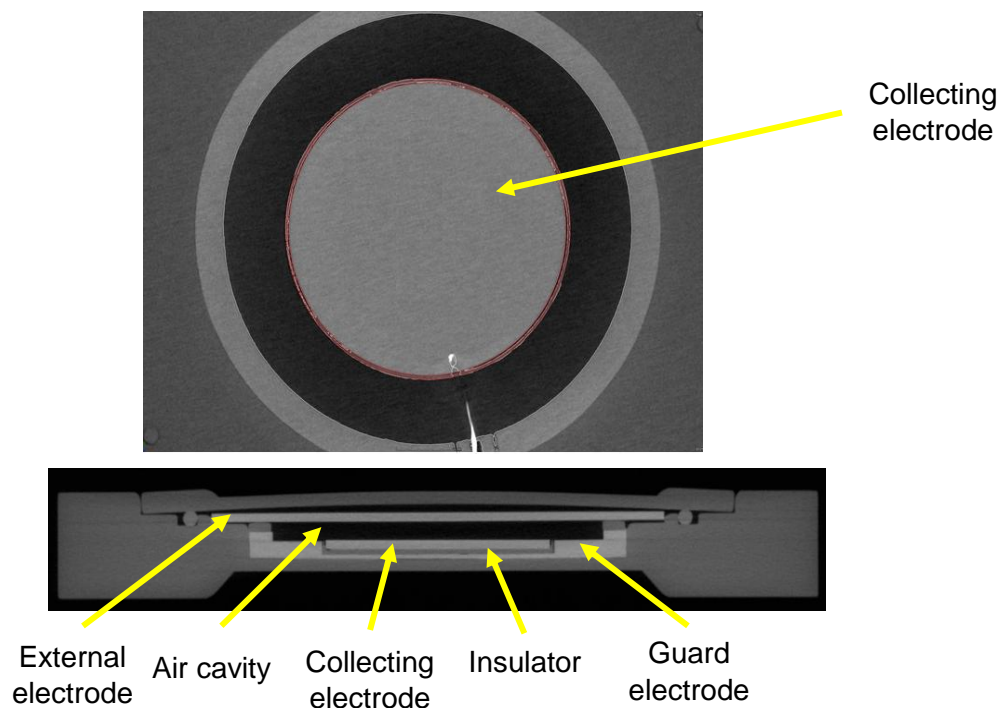


**Figure 6.** 2D X-ray tomography view of one DAP ionization chamber from the front (top) and from a lateral section (bottom).

The two DAP ionization chambers were then evaluated in a 6 MV FFF 10x10 cm<sup>2</sup> beam in terms of long-term stability under irradiation (3 hours time span), noise contribution to signal and polarity correction.

## 2.5 Monte Carlo calculations

A few phase-spaces files (PSF) from different Monte Carlo codes are freely available within the medical physics community [31]. They are then used as input data for simulation and calculations of dosimetric quantities. However, these PSF's have limited size, and assume that all machines are strictly equivalent. It has been shown that this last assumption has some limits, especially for small field sizes less than 1 cm x 1 cm related to spot size shifts and the occlusion effect [32–35].

To overcome this limitation, it was decided to create our own full Monte Carlo 6 MV FFF beam model for the Varian TrueBeam head using the EGSnrc code (2019a version) [36]. With a good knowledge of the TrueBeam head components with data provided by Varian, we were able to accurately model our TrueBeam machine. The linac model was compiled as a shared library to be used as a full beam source in a specific BEAMnrc simulation (ISOURC=23). A model by field size and field shape was created, representing a total of ten configurations (five for square and five for circular fields).

At least five different sets of measurements, moving the jaws from either the smaller or the larger field size, to the field size of interest were performed with a PTW 60019 Microdiamond detector to take into account the jaws position reproducibility. The different experimental PDD and profiles were averaged to get a more reliable reference data set. Then, the hysteresis of jaws is taken into account and minimized. For Monte Carlo simulation, the DOSXYZnrc and DOSRZnrc user codes were used for absorbed dose calculations in the water phantom for respectively square and circular fields. The dose was obtained by scoring the energy deposited in scoring volume dimensions equivalent to the microdiamond detector volume (diameter: 2.2 mm) [37], with a statistical uncertainty better than 0.4 % on central axis.

The validation of each configuration was performed by comparing experimental and calculated percentage depth-doses (PDD) and inline/crossline profiles in the water phantom with a strict 0.5%/0.5mm global gamma-index analysis regarding the metrological expectations. The passing rate for circular and square fields are summarized in **Table .**

**Table 1.** Passing rate for the 0.5%/0.5mm gamma analysis for profiles and PDD small fields defined by jaws and collimators.

Averaged inline/crossline profiles			
Field size side length (mm)	0.5%/0.5mm passing rate (%)	Field size diameter (mm)	0.5%/0.5mm passing rate (%)
5	86.6	5	87.5
7	85.5	7.5	93.8

10	85.3	10	93.8
13	90.3	13	87.5
15	93.9	15	87.5
PDD			
Field size side length (mm)	0.5%/0.5mm passing rate (%)	Field size diameter (mm)	0.5%/0.5mm passing rate (%)
5	100	5	94.1
7	97.1	7.5	94.1
10	100	10	97.1
13	97.1	13	100
15	97.1	15	97.1

### 2.5.1 Graphite to water dose conversion factor $\left[ \frac{D_w(V_{core})}{D_{core}} \right]_{MC}$

As part of primary standards establishment by graphite calorimetry, the graphite to water dose conversion factor  $[D_w(V_{core}) / D_{core}]_{MC}$  is of critical importance in the determination of the absorbed dose area product to water. The DOSRZnrc user code was used to calculate  $D_w(V_{core})$  and  $D_{core}$  of Eq. (1).  $D_{core}$  was calculated in the large section graphite calorimeter core, modelled in detail inside its graphite phantom, placed with its reference point at the reference depth of 10 g.cm<sup>-2</sup> at a source distance of 100 cm. The  $D_w$  term was obtained by scoring the energy deposited in a volume of the same dimensions as the core (15.002 mm radius and 2.919 mm thickness) located at 10 cm depth in the water phantom.

Material cross-section files were generated using the PEGS4 program taken into account the density correction files distributed with the EGSnrc distribution. In particular, the crystalline density of graphite (2.265 g.cm<sup>-3</sup>) to determine the density effect correction, as well as the updated average excitation potentials of graphite and water ( $I = 81$  eV and 78 eV respectively) from ICRU 90 recommendations for stopping-power ratio calculations [38], were taken into account. The density of water was set at 0.998 g.cm<sup>-3</sup> (corresponding to a temperature of 20 °C), in accordance with the updated water-density file distributed with the EGSnrc distribution. The different densities of graphite in the calorimeter and its phantom were all considered by specifically adapting their values in the original density correction file and by regenerating a new cross sections file. In order to take into account a recommendation issued in 2017 by the CCRI (Consultative Committee for Ionizing Radiation) concerning the adoption of re-normalized cross sections for the photoelectric effect, the photon cross section table "mcdx-xcom" was used during the dosimetric calculations. The photon and electron cutoff energies (PCUT and ECUT, respectively) have been taken equal to 1 keV (PCUT = 0.001 MeV and ECUT = 0.512 MeV) to account for the integration of a large fraction of scattered radiation. No variance reduction techniques were applied in the dosimetric calculations. The number of histories was adapted to get a statistical uncertainty around 0.1% for each  $D_{core}$  and  $D_w$  parameter while a type-B uncertainty of 0.55% was considered [24]. The other transport parameters related to the simulation of the absorbed dose calculations are reported in **Table** .

**Table 2.** Modified Monte Carlo transport parameters for graphite to dose conversion factor calculation. Those not mentioned have been taken equal to their default value.

Parameter	Value
Global ECUT (MeV)	0.512
Global PCUT (MeV)	0.001
Brem cross sections	NIST
Bound Compton scattering	On
Pair angular sampling	KM
Rayleigh scattering	On
Electron Impact Ionization	On
Photon cross sections	mcdf-xcom

### 2.5.2 2D dose integral correction $k_{int}$

In the DAP approach, it is necessary to ensure that the charge collection of the DAP ionization chamber is representative of the energy deposited in the calorimeter core. Therefore, the sensitive area of the primary and transfer dosimeters must be as close as possible. Although they were designed to be the same, the manufacturing process introduces slight differences due to machining tolerances. A correction factor called 2D dose integral correction  $k_{int}$  is therefore introduced to account for this effect.

The correction factor  $k_{int}$  is defined as:

$$k_{int} = \frac{\iint_{S_{core}} g(r, \theta) dS}{\iint_{S_{DAP}} g(r, \theta) dS} \quad \#(2)$$

where  $g$ ) is the 2D dose distribution at the reference depth of  $10 \text{ g.cm}^{-2}$  and a source distance of 100 cm, and  $S_{core}$  and  $S_{DAP}$  are respectively the area of the core and of the effective collection area of the DAP ionization chamber. The diameter of the core can be determined using a mechanical caliper. For the DAP chamber collection diameter, the determination was more challenging and was measured by X-ray tomography.

This quantity  $k_{int}$  was calculated with the DOSRZnrc user code in a all-in one calculation with the same parameters as reported in Table . A type B uncertainty of 0.05% coming from tomographic radius determination was added.

### 2.5.3 Monte Carlo modeling of DAP ionization chamber

A Monte Carlo simulation was further carried out with the aim of calculating the theoretical calibration coefficient  $D_w/D_{cav}$  of a DAP ionization chamber.  $D_{cav}$  was obtained by recording the energy deposited in the air cavity of the ionization chamber, modeled in an ideal case without the cover bending, using the DOSRZnrc code. A half-symmetrical cut view of the modeled ionization chamber is shown in **Figure 7** with the sensitive air cavity highlighted in red.

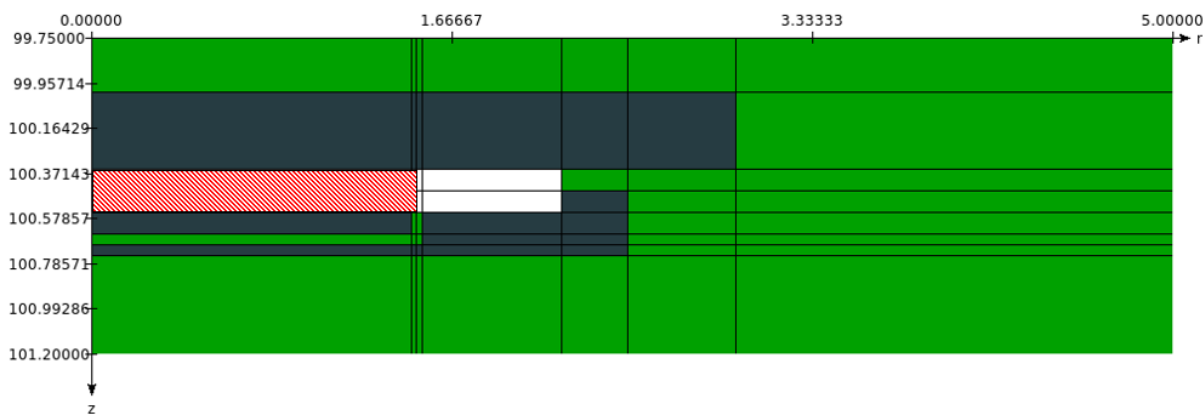


**Figure 7.** Visualization of a 2D section of the DAP ionization chamber with the eggs\_inprz tool. The insulators and the cross-linked polystyrene box are drawn in green, the graphite electrodes drawn in dark gray.

The ionization chamber was placed with its reference point located on the inner surface of the entrance window at 10 cm depth in the water phantom. The dose in water  $D_w$  was recorded in the same region, replacing all the components of the ionization chamber with water. Transport parameters from **Table** were used.

### 3 Results and Discussion

#### 3.1.1 DAP ionization chamber performances as a reference detector

The dosimetric performances evaluation of the two DAP ionization chambers are presented in **Erreur ! Source du renvoi introuvable.**. Additionally, the recombination correction factors are given for the 5 mm and 15 mm diameter field size.

**Table 3.** Characterization measurements of the two DAP ionization chambers performed for a 6 MV FFF beam quality and a 10x10cm<sup>2</sup> field. The recombination correction factors are for the 5 and 15 mm diameters beams.

	Stability under irradiation (%)	Noise contribution to signal (%)	$k_{pol}$	$k_{rec}$ (5 mm)	$k_{rec}$ (15 mm)
DAP1	0.04	0.006	0.9992(0)	1.0016(5)	1.0034(6)
DAP2	0.05	0.008	0.9991(1)	1.0014(5)	1.0034(5)

It was found that the DAP ionization chambers showed an excellent signal stability with deviations less than 0.05% after 3 hours of consecutive measurements and a negligible noise contribution to the measured signal. Also, the polarity correction factor is very close to unity, showing the good metrological quality of the two detectors. The recombination correction factor increases with field size, as expected.

#### 3.1.2 Calibration coefficients $N_{DAP,w}$

Calibration coefficients for the two DAP ionization chambers measured for a 6 MV FFF beam quality are plotted in **Figure 8** for the two collimating systems. Additionally, the values are summarized in **Table 1**. The calibration coefficients seem independent of the beam shape but increase slightly with the field surface (maximum variation of

1.1 % for DAP1 and 1.8% for DAP2 from 19.6 mm<sup>2</sup> to 225 mm<sup>2</sup>), following a linear trend. The slopes of the two DAP chambers are however different preventing the application of a single field size correction factor. Uncertainties are around 0.6% for circular fields and a little bit larger for square fields due to the use of the internal monitor chamber. Whatever the field shape, uncertainties are larger for the smaller field sizes, due to lower temperature rises of the calorimeter core.. With a coverage factor of  $k = 2$ , all calibration coefficients of each chamber are in agreement.

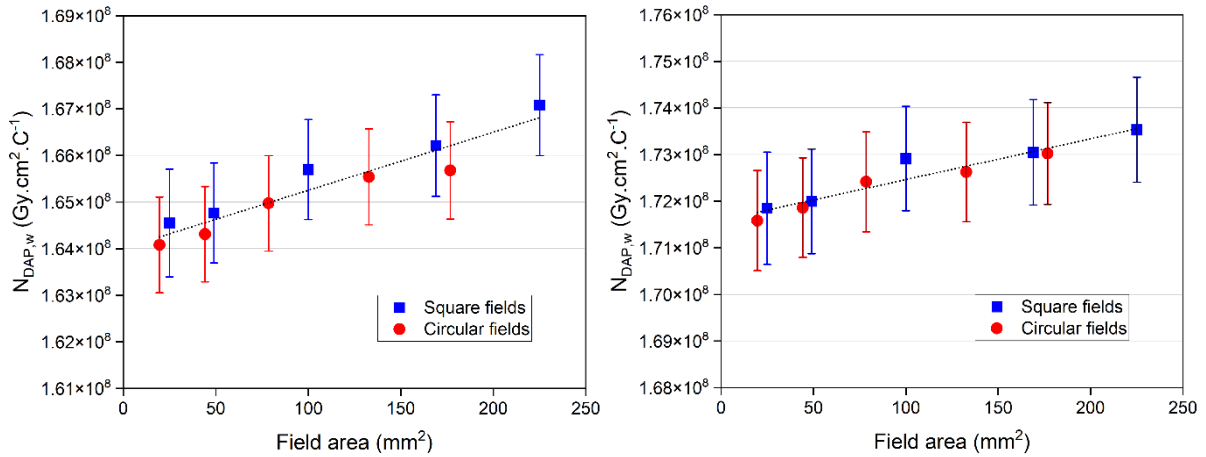


**Figure 8.** Calibration coefficients of the DAP1 (left) and DAP2 (right) ionization chamber as a function of the field area, for square fields (in blue) and circular fields (in red).

**Table 1.** Calibration coefficients  $N_{DAP,w}$  for the two DAP ionization chambers in circular and square fields and a 6 MV FFF beam quality.

6 MV FFF – Circular fields					
Ionization Chamber		DAP1		DAP2	
Area (mm <sup>2</sup> )	Field size diameter (mm)	$N_{DAP,w}$ (Gy.cm <sup>2</sup> .C <sup>-1</sup> )	$u_c$ (%)	$N_{DAP,w}$ (Gy.cm <sup>2</sup> .C <sup>-1</sup> )	$u_c$ (%)
19.6	5	$1.641 \times 10^8$	0.62	$1.716 \times 10^8$	0.63
44.2	7.5	$1.643 \times 10^8$	0.61	$1.719 \times 10^8$	0.62
78.5	10	$1.650 \times 10^8$	0.61	$1.724 \times 10^8$	0.62
132.7	13	$1.655 \times 10^8$	0.61	$1.726 \times 10^8$	0.62
176.7	15	$1.657 \times 10^8$	0.61	$1.730 \times 10^8$	0.62
6 MV FFF – Square fields					
Ionization Chamber		DAP1		DAP2	
Area (mm <sup>2</sup> )	Field size side length (mm)	$N_{DAP,w}$ (Gy.cm <sup>2</sup> .C <sup>-1</sup> )	$u_c$ (%)	$N_{DAP,w}$ (Gy.cm <sup>2</sup> .C <sup>-1</sup> )	$u_c$ (%)
25	5	$1.646 \times 10^8$	0.69	$1.719 \times 10^8$	0.70
49	7	$1.648 \times 10^8$	0.64	$1.720 \times 10^8$	0.65
100	10	$1.657 \times 10^8$	0.64	$1.729 \times 10^8$	0.65
169	13	$1.662 \times 10^8$	0.64	$1.731 \times 10^8$	0.65
225	15	$1.671 \times 10^8$	0.64	$1.735 \times 10^8$	0.64

As an illustration, all the parameters necessary to calculate the DAP to water calibration coefficient  $N_{DAP,w}$  and the associated uncertainties for the 5 mm diameter field size are given in **Table 2**.

**Table 2.** Example of calibration coefficient determination for the 5 mm diameter field size.

	Value	$u$ (%)
$(D_{core/Mon} / Q_{w/Mon})$ ( $Gy \cdot C^{-1}$ )	$2.343 \times 10^7$	0.20
$k_{pol}$	0.9985	0.03
$k_{rec}$	1.0016	0.05
$k_{int}$	1.0003	0.06
$[D_w(V_{core}) / D_{core}]_{MC}$	0.9908	0.57
$S_{core}$ ( $cm^2$ )	7.0700	0.04
$k_i$	1.0000	0.10
$N_{DAP,w}$ ( $Gy \cdot cm^2 \cdot C^{-1}$ )	$1.641 \times 10^8$	0.62

It can be seen that the major uncertainty source of the calibration coefficient comes from the graphite to water dose conversion calculated by Monte Carlo. This parameter is constant within uncertainties lying between 0.9887 and 0.9922 for all the configurations ( $u = 0.57\%$ ). The 2D dose integral correction  $k_{int}$ , is expected to increase with the field size due simply to a larger difference in the energy deposited in the tail region if the collecting surface diameters of the DAP chambers are different from the 15 mm diameter calorimeter core. Those corrections are however very small for the two DAP ionization chambers, in the range [1.0003 to 1.0005] and [1.0007 to 1.0009] for the DAP1 and DAP2 chambers respectively, as the diameters are very close (DAP1: 14.956 mm and DAP2: 14.911 mm).

### 3.1.3 Comparison of calculated dose ratios and measured calibration coefficients

Calculated calibration coefficients are presented in **Figure 9**, with a type-B uncertainty of 0.55%. It can be observed the same trend on the calibration coefficient variation with field size, which could be justified by the perturbation to the particle fluence due to the presence of the detector, depending on its geometry and design [39–42]. Variation of the water/air stopping power ratios between 15 mm and 5 mm field sizes are known to be negligible [43], on the beam axis. However, when looking on the large surface required with the DAP approach, a large amount of low energies electrons is involved. It has been shown [44] that stopping-power ratios show larger variations in the penumbra region, which could also partly explain the calibration coefficient variations.

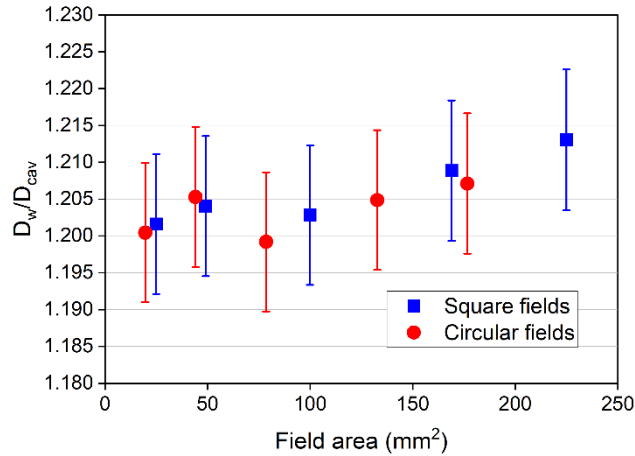


**Figure 9.**  $D_w/D_{cav}$  calculated for an ideal DAP ionization chamber as a function of the field area for square fields (in blue) and circular fields (in red).

To compare the magnitude of the increase, the relative calculated dose ratios and experimental calibration coefficients are normalized to the largest field size for each beam shape, corresponding to a 15 mm field size. Results are shown in **Figure 10**. It can be noticed that the calculated and measured results show similar trends within the uncertainties.

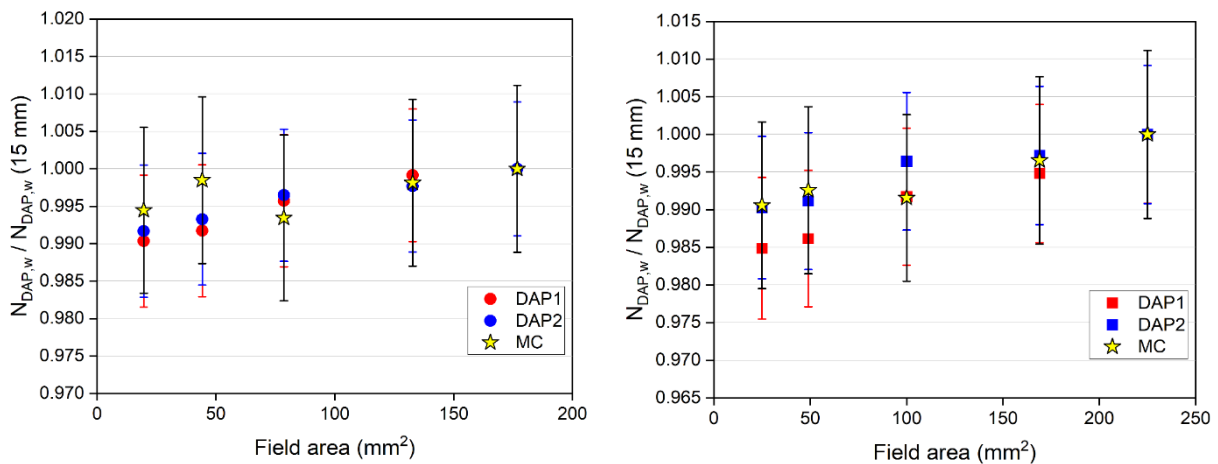


**Figure 10.** Calibration coefficients variations of the two DAP ionization chambers determined by graphite calorimetry and calculated dose ratios of the ideal ionization DAP chamber simulated by Monte Carlo for circular fields (left) and square fields (right), normalized to the largest field size (15 mm side length or 15 mm diameter respectively). The scale is the same for the two graphs.

## 4 Conclusion

Primary standards in small fields by graphite calorimetry in terms of Dose Area Product have been established at the LNE-LNHB for a 6 MV FFF beam for circular and square field sizes from 5 mm to 15 mm (side length and diameter). The field shape independence allows these primary standards to be used independently with stereotactic cones or MLC/jaws. By calibrating a DAP ionization chamber, direct dose measurements can be performed for other radiation delivery modalities. These promising results paves the way to a paradigm shift for small fields dosimetry from DAP primary standards to accelerator commissioning directly introducing the DAP in Treatment Planning Systems (TPS) for OF, as a surrogate of the unsuitable point

dose used so far for small fields. Meanwhile with the actual formalism, a DAP to central axis point dose conversion is possible for a clinical use. This can be done with films through a surface average correction factor using a 2D dose map of the beam. A work is under progress to investigate this method, which is challenging due to the difficulties to measure accurately the penumbra of small radiations fields.

## 5 References

- [1] Leksell L. The stereotaxic method and radiosurgery of the brain. *Acta Chirurgica Scandinavica* 1951;102:316–9.
- [2] Leksell L. Cerebral radiosurgery. I. Gammathalanotomy in two cases of intractable pain. *Acta Chirurgica Scandinavica* 1968;134:585–95.
- [3] Timmerman RD, Hu C, Michalski JM, Bradley JC, Galvin J, Johnstone DW, et al. Long-term Results of Stereotactic Body Radiation Therapy in Medically Inoperable Stage I Non-Small Cell Lung Cancer. *JAMA Oncol* 2018;4:1287–8. <https://doi.org/10.1001/jamaoncol.2018.1258>.
- [4] Herfarth KK, Debus J, Lohr F, Bahner ML, Rhein B, Fritz P, et al. Stereotactic single-dose radiation therapy of liver tumors: results of a phase I/II trial. *J Clin Oncol* 2001;19:164–70. <https://doi.org/10.1200/JCO.2001.19.1.164>.
- [5] Boike TP, Lotan Y, Cho LC, Brindle J, DeRose P, Xie X-J, et al. Phase I Dose-Escalation Study of Stereotactic Body Radiation Therapy for Low- and Intermediate-Risk Prostate Cancer. *J Clin Oncol* 2011;29:2020–6. <https://doi.org/10.1200/JCO.2010.31.4377>.
- [6] INTERNATIONAL ATOMIC ENERGY AGENCY, Absorbed Dose Determination in External Beam Radiotherapy: An International Code of Practice for Dosimetry Based on Standards of Absorbed Dose to Water. Technical Reports Series No 398, IAEA, Vienna 2000.
- [7] Almond PR, Biggs PJ, Coursey BM, Hanson WF, Huq MS, Nath R, et al. AAPM's TG-51 protocol for clinical reference dosimetry of high-energy photon and electron beams. *Med Phys* 1999;26:1847–70. <https://doi.org/10.1118/1.598691>.
- [8] Alfonso R, Andreo P, Capote R, Huq MS, Kilby W, Kjäll P, et al. A new formalism for reference dosimetry of small and nonstandard fields. *Med Phys* 2008;35:5179–86. <https://doi.org/10.1118/1.3005481>.
- [9] INTERNATIONAL ATOMIC ENERGY AGENCY, Dosimetry of Small Static Fields Used in External Beam Radiotherapy : An International Code of Practice for Reference and Relative Dose Determination. Technical Reports Series No 483, IAEA, Vienna 2017.
- [10] Benmakhlouf H, Sempau J, Andreo P. Output correction factors for nine small field detectors in 6 MV radiation therapy photon beams: a PENELOPE Monte Carlo study. *Med Phys* 2014;41:041711. <https://doi.org/10.1118/1.4868695>.
- [11] Francescon P, Cora S, Satariano N. Calculation of  $k(Q(\text{clin}), Q(\text{msr}))$  ( $f(\text{clin}), f(\text{msr})$ ) for several small detectors and for two linear accelerators using Monte Carlo simulations. *Med Phys* 2011;38:6513–27. <https://doi.org/10.1118/1.3660770>.
- [12] Francescon P, Kilby W, Noll JM, Masi L, Satariano N, Russo S. Monte Carlo simulated corrections for beam commissioning measurements with circular and MLC shaped fields on the CyberKnife M6 System: a study including diode, microchamber, point scintillator, and synthetic

microdiamond detectors. *Phys Med Biol* 2017;62:1076–1095. <https://doi.org/10.1088/1361-6560/aa5610>.

- [13] Bassinet C, Huet C, Derreumaux S, Brunet G, Chéa M, Baumann M, et al. Small fields output factors measurements and correction factors determination for several detectors for a CyberKnife® and linear accelerators equipped with microMLC and circular cones. *Med Phys* 2013;40:071725. <https://doi.org/10.1118/1.4811139>.
- [14] Das IJ, Francescon P. Comments on the TRS-483 protocol on small field dosimetry. *Medical Physics* 2018;45:5666–8. <https://doi.org/10.1002/mp.13236>.
- [15] Daures J, Ostrowsky A, Rapp B. Small section graphite calorimeter (GR-10) at LNE-LNHB for measurements in small beams for IMRT. *Metrologia* 2012;49:S174–8. <https://doi.org/10.1088/0026-1394/49/5/s174>.
- [16] Delaunay F, De Carlan L, Daures J, Garcia T, Gouriou J, Le Roy M, et al. LNE-LNHB realization of the unit of the absorbed dose to water under IMRT conditions. *Proc PTB-Dos-56 (Braunschweig) Advanced Metrology for Cancer Therapy* 2011.
- [17] Djouguela A, Harder D, Kollhoff R, Rühmann A, Willborn KC, Poppe B. The dose-area product, a new parameter for the dosimetry of narrow photon beams. *Zeitschrift Für Medizinische Physik* 2006;16:217–27. <https://doi.org/10.1078/0939-3889-00317>.
- [18] Sánchez-Doblado F, Hartmann GH, Pena J, Roselló JV, Russiello G, Gonzalez-Castaño DM. A new method for output factor determination in MLC shaped narrow beams. *Physica Medica* 2007;23:58–66. <https://doi.org/10.1016/j.ejmp.2007.03.002>.
- [19] Fan J, Paskalev K, Wang L, Jin L, Li J, Eldeeb A, et al. Determination of output factors for stereotactic radiosurgery beams. *Med Phys* 2009;36:5292–300. <https://doi.org/10.1118/1.3232217>.
- [20] Underwood TSA, Winter HC, Hill MA, Fenwick JD. Detector density and small field dosimetry: Integral versus point dose measurement schemes. *Medical Physics* 2013;40:082102. <https://doi.org/10.1118/1.4812687>.
- [21] de Chavez R, Jones CE, Charles PH. Integral small field output factor measurements using a transmission ionisation chamber. *Australas Phys Eng Sci Med* 2019;42:235–44. <https://doi.org/10.1007/s13246-018-0716-x>.
- [22] Niemelä J, Partanen M, Ojala J, Sipilä P, Björkqvist M, Kapanen M, et al. Measurement and properties of the dose–area product ratio in external small-beam radiotherapy. *Phys Med Biol* 2017;62:4870–4883. <https://doi.org/10.1088/1361-6560/aa6861>.
- [23] Niemelä J, Partanen M, Ojala J, Kapanen M, Keyriläinen J. Dose-area product ratio in external small-beam radiotherapy: beam shape, size and energy dependencies in clinical photon beams. *Biomed Phys Eng Express* 2021. <https://doi.org/10.1088/2057-1976/abf6aa>.
- [24] Pimpinella M, Caporali C, Guerra AS, Silvi L, De Coste V, Petrucci A, et al. Feasibility of using a dose-area product ratio as beam quality specifier for photon beams with small field sizes. *Phys Med* 2018;45:106–16. <https://doi.org/10.1016/j.ejmp.2017.12.012>.
- [25] Dufreneix S, Bordy J-M, Daures J, Delaunay F, Ostrowsky A. Construction of a large graphite calorimeter for measurements in small fields used in radiotherapy. 16th International Congress of Metrology, EDP Sciences; 2013, p. 05006. <https://doi.org/10.1051/metrology/201305006>.

- [26] Dufreneix S, Ostrowsky A, Roy ML, Sommier L, Gouriou J, Delaunay F, et al. Using a dose-area product for absolute measurements in small fields: a feasibility study. *Phys Med Biol* 2015;61:650–662. <https://doi.org/10.1088/0031-9155/61/2/650>.
- [27] Joint Committee for Guides in Metrology (JCGM), Evaluation of Measurement data - Guide to the Expression of Uncertainty in Measurement, JCGM 100:2008 (GUM 1995 with minor corrections). 2008.
- [28] Daures J, Ostrowsky A. New constant-temperature operating mode for graphite calorimeter at LNE-LNHB. *Phys Med Biol* 2005;50:4035–52. <https://doi.org/10.1088/0031-9155/50/17/008>.
- [29] Delaunay F, Gouriou J, Daures J, Le Roy M, Ostrowsky A, Rapp B, et al. New standards of absorbed dose to water under reference conditions by graphite calorimetry for  $^{60}\text{Co}$  and high-energy x-rays at LNE-LNHB. *Metrologia* 2014;51:552–62. <https://doi.org/10.1088/0026-1394/51/5/552>.
- [30] Renaud J, Palmans H, Sarfehnia A, Seuntjens J. Absorbed dose calorimetry. *Phys Med Biol* 2020;65:05TR02. <https://doi.org/10.1088/1361-6560/ab4f29>.
- [31] Capote R, Jeraj R, Ma CM, Rogers DWO, Sanchez-Doblado F, Sempau J, et al. Phase-space database for external beam radiotherapy Summary report of a consultants' meeting. International Atomic Energy Agency (IAEA): 2006.
- [32] Czarnecki D, Wulff J, Zink K. The influence of linac spot size on scatter factors. *Metrologia* 2012;49:S215–S218. <https://doi.org/10.1088/0026-1394/49/5/S215>.
- [33] Wang LLW, Leszczynski K. Estimation of the focal spot size and shape for a medical linear accelerator by Monte Carlo simulation. *Med Phys* 2007;34:485–8. <https://doi.org/10.1118/1.2426407>.
- [34] Scott AJD, Nahum AE, Fenwick JD. Monte Carlo modeling of small photon fields: quantifying the impact of focal spot size on source occlusion and output factors, and exploring miniphantom design for small-field measurements. *Med Phys* 2009;36:3132–44. <https://doi.org/10.1118/1.3152866>.
- [35] Ghazal M, Westermarck M, Kaveckyte V, Carlsson-Tedgren Å, Benmakhlof H. 6-MV small field output factors: intra-/intermachine comparison and implementation of TRS-483 using various detectors and several linear accelerators. *Medical Physics* 2019;46:5350–9. <https://doi.org/10.1002/mp.13830>.
- [36] Kawrakow I, Mainegra-Hing E, Rogers DWO, Tessier F, Walters BRB. The EGSnrc Code System: Monte Carlo simulation of electron and photon transport. Technical Report PIRS-701. National Research Council Canada 2019.
- [37] Marinelli M, Prestopino G, Verona C, Verona-Rinati G. Experimental determination of the PTW 60019 microDiamond dosimeter active area and volume. *Medical Physics* 2016;43:5205–12. <https://doi.org/10.1118/1.4961402>.
- [38] ICRU 90 -Small Field Dosimetry. *Journal of the International Commission on Radiation Units and Measurements* 2014;14:31–53. <https://doi.org/10.1093/jicru/ndx012>.
- [39] Bouchard H, Kamio Y, Palmans H, Seuntjens J, Duane S. Detector dose response in megavoltage small photon beams. II. Pencil beam perturbation effects. *Medical Physics* 2015;42:6048–61. <https://doi.org/10.1118/1.4930798>.

- [40] Fenwick JD, Georgiou G, Rowbottom CG, Underwood TSA, Kumar S, Nahum AE. Origins of the changing detector response in small megavoltage photon radiation fields. *Phys Med Biol* 2018;63:125003. <https://doi.org/10.1088/1361-6560/aac478>.
- [41] Andreo P, Benmakhlouf H. Role of the density, density effect and mean excitation energy in solid-state detectors for small photon fields. *Phys Med Biol* 2017;62:1518–1532. <https://doi.org/10.1088/1361-6560/aa562e>.
- [42] Benmakhlouf H, Andreo P. Spectral distribution of particle fluence in small field detectors and its implication on small field dosimetry. *Medical Physics* 2017;44:713–24. <https://doi.org/10.1002/mp.12042>.
- [43] Andreo P, Brahme A. Stopping power data for high-energy photon beams. *Phys Med Biol* 1986;31:839–58. <https://doi.org/10.1088/0031-9155/31/8/002>.
- [44] Eklund K, Ahnesjö A. Fast modelling of spectra and stopping-power ratios using differentiated fluence pencil kernels. *Phys Med Biol* 2008;53:4231–4247. <https://doi.org/10.1088/0031-9155/53/16/002>.